






Original Article


Effect of seepage-induced erosion on soil macropore structure


HUANG Wen-bo¹  <https://orcid.org/0000-0002-2552-4527>; e-mail: 201811601008@stu.hebut.edu.cn

HUANG Da^{2*}  <https://orcid.org/0000-0002-2795-1354>;  e-mail: dahuang@hebut.edu.cn

GAO Yi-kang¹  <https://orcid.org/0009-0003-7402-0645>; e-mail: rprcv8@163.com

LIU Yang¹  <https://orcid.org/0000-0003-0655-3848>; e-mail: 201911601006@stu.hebut.edu.cn

LI Zhao¹  <https://orcid.org/0000-0001-7784-6985>; e-mail: 202011601014@stu.hebut.edu.cn

MENG Qiu-jie¹  <https://orcid.org/0000-0002-8753-6718>; e-mail: 201621601006@stu.hebut.edu.cn

* Corresponding author

¹ School of Civil and Transportation Engineering, Hebei University of Technology, Tianjin 300401, China.

² College of Geology Engineering and Geomatics, Chang'an University, Xi'an 710054, China.

Citation: Huang WB, Huang D, Gao YK, et al. (2023) Effect of seepage-induced erosion on soil macropore structure. Journal of Mountain Science 20(11). <https://doi.org/10.1007/s11629-023-8082-x>

© Science Press, Institute of Mountain Hazards and Environment, CAS and Springer-Verlag GmbH Germany, part of Springer Nature 2023

Abstract: Internal erosion is one of the important factors causing geological disasters. The microstructure of soil can change with seepage erosion, resulting in changes in the hydraulic and mechanical properties of the soil. The evolution of seepage erosion is investigated with X-ray computed tomography (CT) in this study. The change in macropore structure characteristics during the seepage erosion test is quantified and the influence of seepage erosion on soil deformation is analyzed. Moreover, a pore network model (PNM) is established for the specimens and the evolution of the connected pore size characteristics is assessed. The results show that the macropore structure is significantly affected by seepage erosion, especially in terms of the porosity and pore geometry characteristics. The changes in macropore structure characteristics are most obvious in the lower part of the specimen. The influence of seepage erosion on the pore size distribution (PSD) and soil deformation is heterogeneous and closely dependent on the spatial location of the soil. Moreover, seepage erosion enhances macropore

connectivity and has a directional impact on macropore orientation. These findings can provide a reference for the theoretical modeling and numerical simulation of the seepage erosion and improve the understanding of the seepage erosion evolution in engineering practice.

Keywords: Seepage erosion; Heterogeneity; Macropore structure; Pore size distribution; Microstructure; CT scanning

1 Introduction

Hydraulic actions, such as rainfall, fluctuations in reservoir water level, freezing–thawing cycles and wetting–drying cycles, are the main factors affecting geological hazards, including landslides, dam breaks, soil erosion, and debris flows (Korup 2004; Huang 2009; Nowamooz et al. 2016; Luo et al. 2019; Liu et al. 2020; Qin et al. 2021). Seepage erosion in soil slopes, slope deposits, and reactivated old landslides significantly decreases their stability and induces landslides (Crosta and Prisco 1999; Fox and Wilson

Received: 18-May-2023

Revised: 15-Aug-2023

Accepted: 10-Oct-2023

2010; Flores-Berrones et al. 2011; Pan et al. 2017; Lei 2021). Among 11192 surveyed dams, 136 dams experienced dysfunction, 46% of which was related to seepage erosion (Foster et al. 2000). The hydraulic properties and mechanical conditions can be changed with long-term erosion. Moreover, the structural surfaces in slopes and dams, such as soil–rock interfaces or soil–structure interfaces, are the dominant seepage surfaces that are vulnerable to seepage erosion and can control the overall stability (Chu-Agor et al. 2008; Kim et al. 2019; Huang et al. 2021). Seepage erosion is especially dangerous because it is imperceptible and persistent (Flores-Berrones et al. 2011; Zuo et al. 2020). Therefore, it is crucial to investigate the evolution and failure mechanisms of seepage erosion.

Seepage erosion can be divided into four types: suffusion, backward erosion, contact erosion and concentrated leak erosion (Fell and Fry 2007). Each erosion type shows different erosion evolution characteristics and failure mechanisms, which depend on the soil structure characteristics, hydraulic conductions and stress state, such as grain size distribution (GSD), soil porosity and seepage direction (Richards and Reddy 2007; Chang and Zhang 2013; Liu et al. 2019; Chen et al. 2021; Zhu et al. 2022). Moffat et al. (2011) investigated the susceptibility of four widely graded soils to internal erosion and revealed novel insights into the spatial and temporal progression of seepage erosion. Their results indicated that the erosion evolution is governed by both the effective stress and hydraulic gradient and that a drastic decrease in the local hydrometric gradient suggests the onset of instability. Richards and Reddy (2012) investigated the influence of different factors on the initiation and evolution of different erosion failure types by a true triaxial permeameter apparatus and indicated that the influence of intermediate and minor principal stresses on seepage erosion initiation is insignificant. Through a series of suffusion tests by a triaxial permeameter and a one-dimensional seepage permeameter, Ke and Takahashi (2014) revealed that the porosity of a sample would increase with the progress of suffusion, resulting in a reduction in soil strength. Nevertheless, previous studies mostly investigated seepage erosion on the macroscale with macroscopic hydraulic measurements, such as measurements of hydraulic conductivity, critical hydraulic gradient and eroded soil mass, which cannot directly reflect changes in soil

structure. The specimens showed significant transverse heterogeneities (i.e., perpendicular to the flow direction) and longitudinal heterogeneities (i.e., parallel to the flow direction) in seepage erosion tests (Moffat et al. 2011; Sail et al. 2011; Huang et al. 2021). This cannot be quantified by traditional macroscopic measurements. Furthermore, it is difficult to obtain the continuous evolution of seepage erosion because the measuring methods are destructive (Starkloff et al. 2017). Therefore, it is imperative to investigate the change in soil microstructure during the evolution of seepage erosion.

With the in-depth study of geomaterials, researchers have concluded that the microstructure of soil significantly affects its hydraulic and mechanical properties and that it is essential to quantitatively investigate the change in soil microstructure (Chang and Zhang 2013; Wang et al. 2019; Guo and Cui 2020; Zhao et al. 2020; Wang et al. 2021b). X-ray computed tomography (CT), an effective nondestructive detection technology, makes it possible to quantify soil microstructure at the pore scale and acquire the three-dimensional microstructure of soils (Starkloff et al. 2017; He et al. 2020; Kido et al. 2020). There have been numerous recent studies of changes in soil microstructure based on CT technology, including water retention and solute transport, strain localization, particle morphological features and so on (Luo et al. 2010; Manahiloh and Meehan 2017; Zhao et al. 2017; Meng et al. 2018; Kido et al. 2020). Nevertheless, few experimental investigations on the change in soil pore structure with seepage erosion have been reported in the literature. Based on the spatiotemporal evolution of clogging and unclogging at the microscopic scale, Bianchi et al. (2018) revealed that the permeability jumps during internal erosion could be attributed to flow path reorganization. Through images obtained from CT, Nguyen et al. (2019) demonstrated that a preferential flow path existed at the periphery of a sample during seepage erosion testing, which makes it difficult to characterize the mechanical properties of soil material after erosion with a small-scale device. Hence, further investigation and understanding of seepage erosion at the microscale is indispensable and significant.

In the present study, CT scanning experiments were performed during seepage erosion testing to investigate the influences of seepage erosion on the soil macropore structure. The visualization and

quantification of macropore structure was conducted with AVIZO software. The changes in the pore structure characteristics and pore size distribution (PSD) during seepage erosion development were calculated and analyzed. Moreover, a pore network model (PNM) of the specimen was established, and the influence of seepage erosion on the connected pore size characteristics was assessed. This study provides a reference and supplement for discrete element method numerical simulations and macroscale seepage erosion tests and enhances the understanding of the seepage erosion evolution process.

2 Experimental Method

2.1 Testing apparatus

In this study, a permeameter was designed and used to investigate the evolution of seepage erosion under unidirectional seepage flow. A schematic diagram of the apparatus is shown in Fig. 1. It consists of a water tank, a permeameter cell, a soil collection unit, a water collection unit and a data acquisition system. The water is sent directly into the water tank to provide a constant head drop. The permeameter cell is made of a cylindrical Perspex tube and is fitted with one group of pore water pressure transducers (PWPTs). The permeameter cell is 70 mm in diameter and 180 mm in height. The perforated steel plate with one array of 4 mm diameter round holes is installed on the base pedestal. The eroded soil collection system consists of a conical drainage, a detachable container and an electronic balance. The detachable container is replaceable during the test to investigate the eroded soil mass under different water head drops. The water collection unit includes an acrylic water container, a downstream reservoir and an electronic balance. To maintain a constant water head, the water level of the downstream reservoir is slightly higher than the bottom of the specimen. The data monitoring and recording of PWPTs and electronic balance are automatically performed by the data acquisition system.

2.2 Test materials

The tested soil (TS) material was remolded by mixing gravelly granite (GG) and quartz sand (QS) to

ensure repeatable and predictable performance. GG is the coarse-grained matrix, and QS is the fine-grained matrix. Fig. 2 shows their GSDs together with that of the mixture, and the properties of TS are presented in Table 1. The tested soil is gap-graded soil, which is more prone to internal erosion due to the lack of certain grain sizes (Wan and Fell 2008). The potential

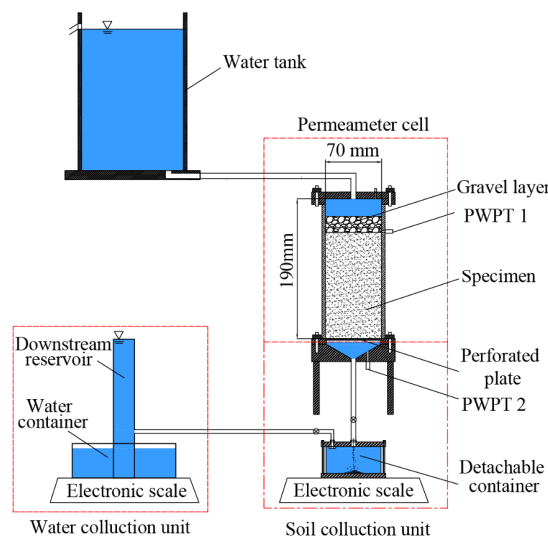


Fig. 1 Schematic diagram of test apparatus.

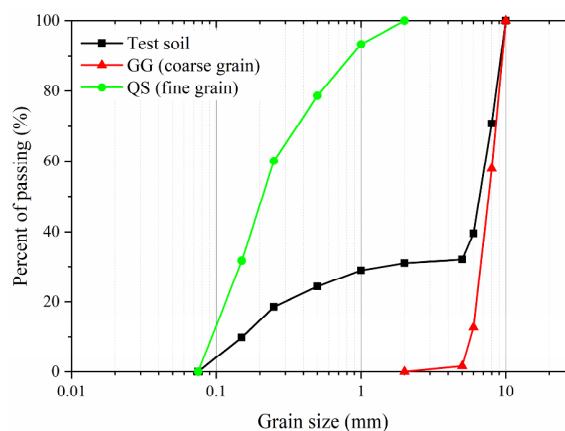


Fig. 2 Particle size distribution of tested soil.

Table 1 Grains size distribution parameters

Properties	GG	QS	TS
Specific gravity, G_s	2.71	2.68	2.70
Uniformity coefficient, C_u	2.77	1.38	41.20
Fines content (%)	-	-	31
D_{15}/d_{85}	-	-	8.97
$(H/F)_{min}$	-	-	0.099

Notes: D_{15} is the maximum grain size of smallest 15 % of coarse matrix (GG); d_{85} is the maximum grain size of smallest 85% of fine matrix (QS). H is the mass fraction over a range of grain diameter d to $4d$; F is the mass passing at the lower limit of the interval grain size d . TS, tested soil.

vulnerability of internal erosion is controlled by the geometric properties of the soil composition. TS is identified as internal instability according to the geometric criteria of Kezdi (1979), Kenney and Lau (1985) and Fannin and Moffat (2006). Hence, internal erosion can be triggered when the hydraulic gradient reaches the critical value.

2.3 Test procedure

The preparation phase includes specimen preparation and saturation. To prevent soil segregation, the specimen was prepared by moist tamping with 6.5% water content. Each tested specimen was 150 mm in height and 70 mm in diameter. The soil was tamped with three layers, and each layer was 50 mm. Dry density control is employed at each layer to improve the accuracy and repeatability of the test. The soil is compacted manually to the target height layer by layer with the compaction hammer. A gravel layer was placed at the top of the specimen to prevent the impact of incoming flow and to ensure uniform flow through the specimen. The differential water-head method was performed to saturate the specimen (Suits et al. 2011). The deaired water slowly flowed into the specimen from bottom to top by increasing the water head, and the change in water level was sufficiently slow (i.e., 5 cm per 1 h). This approach prevents soil segregation and achieves good saturation at the termination of the saturation process.

After the preparation phase, the seepage erosion test was initiated. The increase in the water head drop was performed by a multistage process to the final value. Based on several trial tests, the increment of the hydraulic gradient of each step was selected to be a small value (i.e., $\Delta i_{av} = 0.2 \sim 0.5$). This was to investigate the evolution of seepage erosion accurately and to prevent potential soil destabilization due to the sharp increase in the hydraulic gradient. The hydraulic gradient was increased to a higher level

when the outflow rate remained constant and there was no further eroded soil loss. To ensure sufficient seepage stability, the duration of each stage was approximately 45-90 min. At the end of the stage, CT scanning was performed, and the detachable container was replaced. The tests were terminated when (1) the specimen could not sustain any further increase in the hydraulic gradient and erosion failure was triggered or (2) the maximum hydraulic gradient of the device was applied. The pore water pressure and flux were collected automatically during the test. The actual eroded soil mass was calculated by oven-dried soil particles collected in the detachable container. It is helpful to assess and calibrate subsequent image processing.

Four scans were performed with specimens by high-resolution CT (YXLON-FF35, Germany), corresponding to the different erosion evolution stages during the seepage erosion test (Fig. 3). Scan 1 is obtained after the completion of saturation; Scan 2 is obtained at the termination of the critical hydraulic gradient, implying the onset of erosion but not significant eroded soil loss; Scan 3 and 4 are performed after the soil has undergone erosion, corresponding to different hydraulic gradients and erosion degrees. CT scanning parameters were a working voltage of 200 kV and an operating current of 220 μ A. The container is made of transparent acrylic material, which may cause beam hardening close to the sidewall (Starkloff et al. 2017). Hence, the 1-mm-thick copper plate covered the detector to improve the image quality and attenuate the beam-hardening phenomenon. During the scan test, the sample table was rotated 360°, and the scanning rate (rotation angle of the sample table) was 0.33°. A total of 1080 radiographs of the sample with a discretization of 2048 \times 2048 pixels were obtained in each scan. The corresponding spatial resolution (i.e., a voxel) was 0.1 mm \times 0.1 mm \times 0.1 mm (x, y, z). The acquisition time of each scan was approximately 60 min.

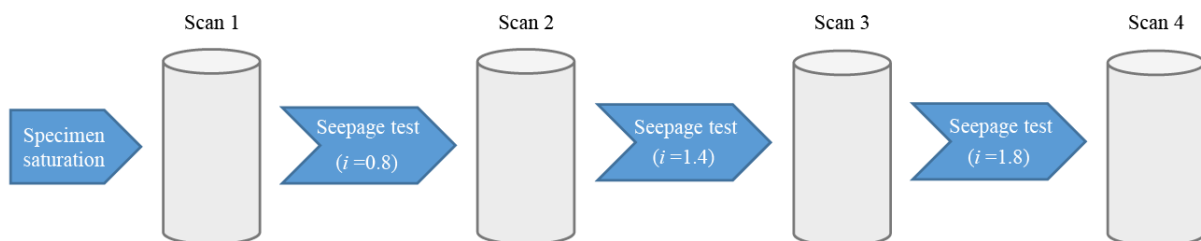


Fig. 3 Process of the seepage erosion test with the four successive scans. i is the hydraulic gradient during the test.

2.4 Image processing and PNM extraction

After CT scanning, CT images were further processed. Image processing was performed in AVIZO software, including region of interest (ROI) delimiting, noise filtering, image segmentation and 3D reconstruction. First, the voxels outside the soil specimen were removed. The size of the images after cropping was $700 \times 700 \times 1500$ voxels, corresponding to physical dimensions of $70 \text{ mm} \times 70 \text{ mm} \times 150 \text{ mm}$. Then, the clipped image was divided into three parts in the vertical direction, and three ROIs were selected, which were called Top, Middle and Bottom, corresponding to the upstream, midstream and downstream parts in the seepage process (i.e., the upper, middle and lower parts of the specimen). The determined ROI size was a cylindrical region with 700 voxels in diameter and 500 voxels in height. To reduce the noise and weaken its negative influence on the quantitative analysis of images, the images were filtered by median filtration, which can remove the noise and retain the edges of the pores and matrix (Bianchi et al. 2018; Wang et al. 2019).

Due to the presence of a partial volume effect (i.e., the gray value of a voxel is selected to be the mean gray value when the voxel includes both the pore and matrix) and the $100 \mu\text{m}$ resolution of the 3D images, the pores with pore diameters greater than $100 \mu\text{m}$ could be distinguished in this study (Fan et al. 2020; Kido et al. 2020). This resolution can quantitatively investigate macropores with diameters $> 100 \mu\text{m}$ (Dragila 2005; Jarvis 2020). To separate the soil matrix and pores, the grayscale images were binarized into macropores and matrix using both threshold segmentation and fast watershed segmentation. The unique threshold cannot be accurately selected, resulting in insufficient segmentation or oversegmentation of macropores due to blurred edges and partial volume effects (Videla et al. 2006; Li et al. 2019). The fast watershed segmentation technique is a mathematical morphological algorithm that has excellent sensitivity to weak edges and resists interference of image noise. Fast watershed segmentation is an effective remedial method to alleviate the insufficient segmentation or oversegmentation of images. Finally, the reconstruction and visualization of the 3D structure model of the pores and matrix were obtained using a fast watershed algorithm based on the binary images (Fig. 4). Fig. 5 shows the volume of cumulative soil

loss measured by direct weighing and image processing. The volume of cumulative soil loss measured by image processing (i.e., the change in pore volume measured by image processing) agrees well with the actual volume of cumulative soil loss, suggesting that the proposed image processing approach can reflect the change in macropore structure during the seepage erosion process in this study.

The PNM can accurately characterize the connected pore structure and morphological properties, which is a suitable and essential supplementary means for studying the permeability of soil. It has been widely employed in geotechnical engineering, petroleum and natural gas engineering (Simms and Yanful 2005; Gharedaghlou et al. 2018; Hu et al. 2020; Daneshian et al. 2021). The PNM consists of two distinct elements, namely, pores and throats, corresponding to the larger soil-connected pores and the narrow sections that control the fluid flow between the pores, respectively. The PNM is established by the following steps. (1) The connectivity analysis is first conducted according to the binary image, and the connected pores of the specimen are identified and extracted. (2) The pores are labeled and separated, and the pore distances are calculated. (3) The skeleton of the PNM is extracted, and the pores and pore throats are separated and marked.

2.5 Quantitative measures of macropore structure

Quantitative measures of the macropore structure characteristics, including macroporosity, connectivity, surface area of macropores, fractal dimension and shape factor, were obtained by the computation module in AVIZO. The definitions and explanations of macropore characteristics are shown in Table 2. Connectivity is an important indicator in the analysis of the spatial morphology of soil macropores. It can be evaluated using the connected ratio C and coordinate number C_N . All macropores are connected pores if C equals 1, and no percolating macropores (connected pores) exist if C equals 0. The fractal dimension D_d and dip angle can reflect the heterogeneity of the macropore spatial distribution. A larger fractal dimension indicates a more complex macropore structure. The dip angle distribution intuitively shows the macropore development trend.

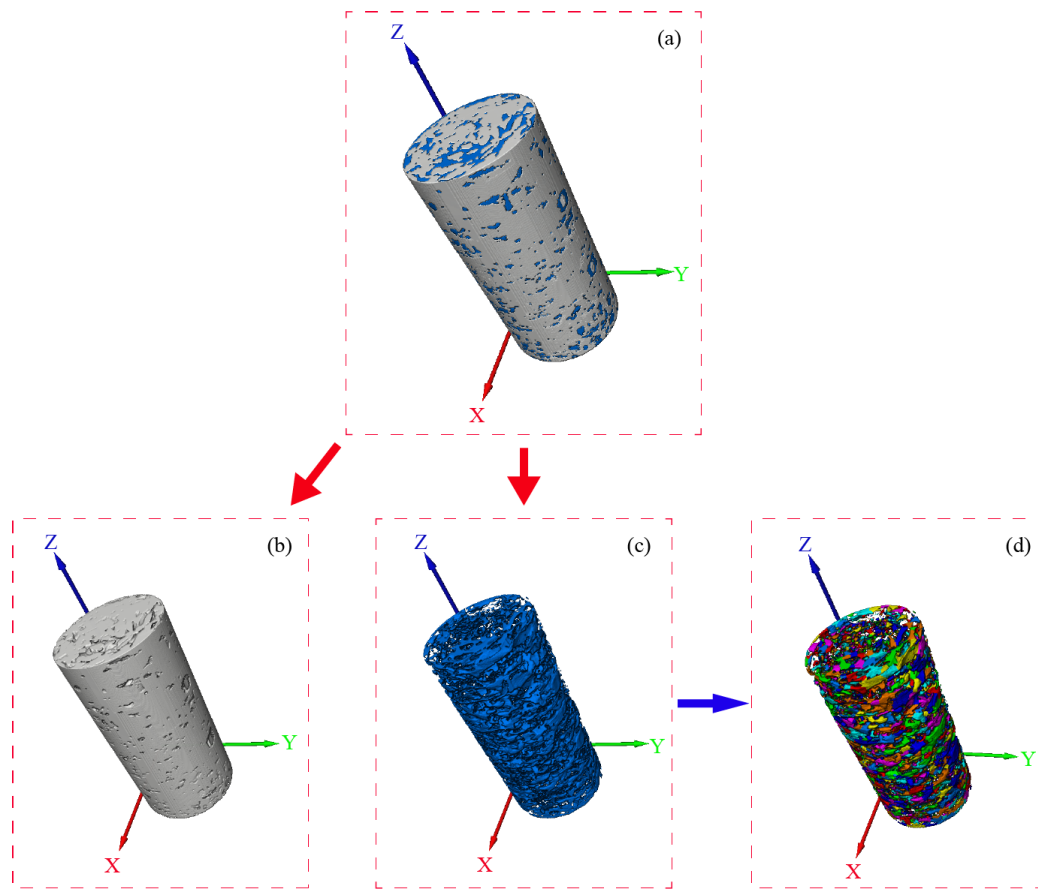


Fig. 4 3D digital model. (a) 3D data volume rendering of specimen; (b) Soil matrix model; (c) Pore model; (d) Separation of the pore model

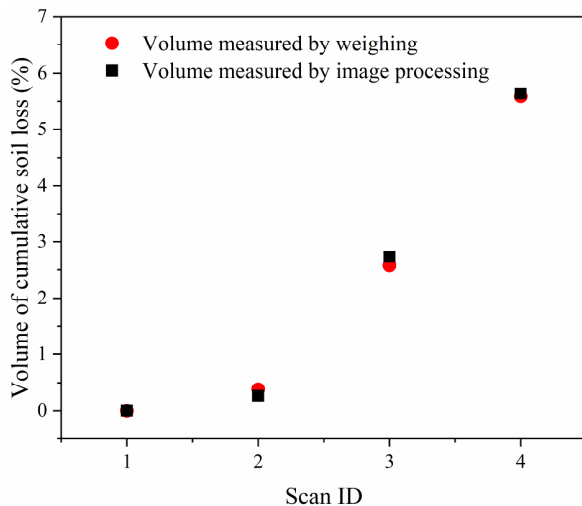


Fig. 5 Volume of cumulative soil loss measured by weighing and image processing.

Finally, the PSD is one of the essential characteristics of the soil macropore structure that significantly affects the hydraulic and mechanical properties (Zhao et al. 2017; Guo and Cui 2020).

3 Results and Discussions

3.1 Development of the erosion process

Fig. 6 shows the grayscale image and binary image of the vertical section of a specimen. The spatial distribution of the macropores in the specimen is heterogeneous. This is attributed to the inhomogeneous distribution of coarse grains, which is inevitable during specimen preparation. Due to the minor loss of fine particles during the saturation phase, the bottom of the specimen has many macropores with larger diameters. The edge of the specimen has a denser pore distribution than its interior as a result of the boundary effect. The soil at the interface has a different pore structure than the interior of the soil and usually has a higher porosity (Kim et al. 2019). Note that the initial macroporosity (Scan 1) of the specimen is approximately 10%, which is far less than its actual porosity (approximately 30%). This is in agreement with the existing research

Table 2 Parameters and definitions/explanations of the macropore

Parameter	Symbol	Formula	Explanations
Porosity	n	V_p/V	V_p and V are the pore volume and the total volume of image, respectively (mm ³)
Connected porosity	n_c	V_c/V	V_c and V are the connected pore volume and the total volume of image
Connected ratio	C	V_c/V_T	V_c and V_T are the connected pore volume and the total pore volume
Fractal dimension	D_d	$\lim_{s \rightarrow 0} \frac{\log N(s)}{\log(1/s)}$	s is side length of the cubic box, $N(s)$ is the smallest number of cubic boxes that can cover the point (pores in this case)
Shape factor	SF	$A_{3D}^3 / 36\pi V_{3D}^2$	A_{3D} is the surface area of pore (mm ²), V_{3D} is the volume of pore (mm ³)
Tortuosity	τ	L_T/L_0	L_T is the actual path length of fluid flow, L_0 is the linear length between start and end point of sample
Dip angle	θ	$\sin^{-1} \frac{ z_i - z_j }{\sqrt{(x_i - x_j)^2 + (y_i - y_j)^2 + (z_i - z_j)^2}}$	Where (x_i, y_i, z_i) and (x_j, y_j, z_j) are the coordinates of the start and end points of pore long axis
Coordinate number	C_N	-	The number of branches connected with the pore

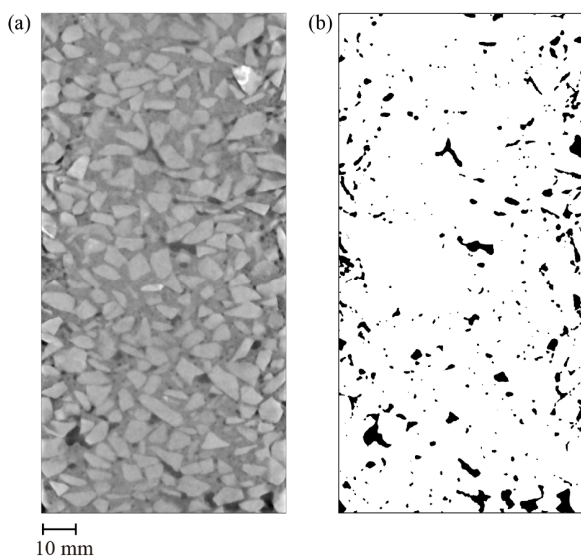


Fig. 6 Vertical cross-section of (a) original image and (b) binary image.

results (Buczko et al. 2006; Cheik et al. 2019). Due to the limits of sample size, detector resolution and step size of CT scanning, mesopores and micropores cannot be detected, and consequently, the porosity obtained by image recognition is usually less than the actual value. According to previous studies, however, a pore >80 μm in diameter is defined as a macropore, and macropores control the water content movement in soil (Dragila 2005; Zhou et al. 2018; Budhathoki et al. 2022). The mesopores and micropores contribute insignificantly to the soil permeability (Lin et al. 1995; Wang et al. 2019). Therefore, the distribution and

evolution of macropores can reflect the changes in the soil pore structure and is highly pertinent in this study.

The 3D reconstructed macropore structure and the variation in porosity and hydraulic conductivity are shown in Fig. 7. There is little variation in macroporosity between Scans 1 and 2, and no noticeable erosion is observed. The hydraulic conductivity of the specimen increases slightly. With the development of seepage erosion, the pore structure changes appreciably in Scans 3 and 4, and some small pores merge into large pores. The porosity and hydraulic conductivity increase significantly, and these parameters are clearly positively correlated. As demonstrated by the vertical and horizontal sections of the specimen (Figs. 8 and 9), the macropores at the bottom of the specimen increase slightly in Scan 2 compared with Scan 1, but no noticeable soil mass loss or erosion is observed inside the specimen. In Scans 3 and 4, the seepage erosion in the entire specimen continuously develops in the vertical direction and is most obvious at the edge of the specimen. The erosion starts from the edge of the specimen and develops nonuniformly from the bottom to the top of the specimen. In Scan 3, the pores at the center of the specimen change less, and the large pores are concentrated at the sidewall of the specimen, particularly at the lower part of the specimen. This is probably attributed to the fact that the soil-structure interface is the preferential seepage channel in the soil mass, and the pore structure of the

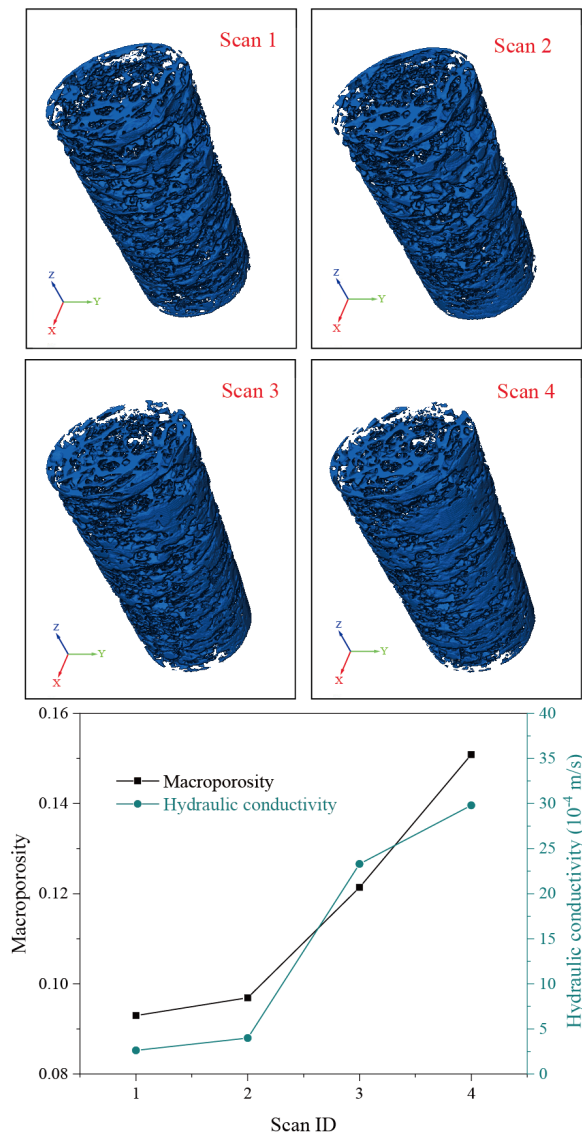


Fig. 7 Three-dimensional total pore structure model of the four successive scans and corresponding macroporosity and hydraulic conductivity.

soil at the interface is usually looser. It sustains a higher hydraulic shear stress and thus is more susceptible to erosion (Kim et al. 2019; Huang et al. 2021). In Scan 4, the erosion process is more intense, and soil erosion develops randomly in the vertical or horizontal direction. The middle part of the specimen shows more obvious and more dispersed soil mass loss than its upper part. The lower part of the specimen shows more extensive soil erosion, and large pores gradually spread at the bottom of the specimen. The development of seepage erosion significantly changes the soil pore structure and is spatially (vertically and horizontally) heterogeneous and asynchronous.

Previous macroscopic experimental studies concluded that the evolution of seepage erosion is not continuous but exhibits the repetition of suffusion and clogging (Bendahmane et al. 2008; Ke and Takahashi 2014). It is difficult to perform dynamic CT scanning during the tests. Moreover, the process of erosion and clogging of the mesopores and micropores cannot be detected due to the limitation of CT scanning resolution in this study, and it is consequently impracticable to quantitatively analyze these pores. However, this can be demonstrated visually by an analysis of CT images. Fig. 10 shows the change in macropore structure during seepage erosion. The macropore structure changes less when the hydraulic gradient is low. The original pores gradually expand and interconnect, and new pores are constantly generated in the specimen with the migration of soil particles during the test. The seepage channel subsequently enlarges, which is attributed to the process of suffusion. Due to the small size of some seepage channels, fine particles cannot pass through and deposit in them. The clogging is subsequently triggered, and some pores gradually decrease or even disappear during the test. In particular, the macroporosity decreases at the local position of the specimen, which also indicates the occurrence of clogging (Fig. 11). The location of suffusion and clogging is constantly changing, which depends on the distribution of coarse grains and the change in hydraulic conditions.

3.2 Quantitative measures of seepage erosion effects on macropore structure characteristics

3.2.1 Change in macroporosity distribution

To quantitatively investigate the influence of seepage erosion on the soil pore structure, the specimen macroporosity in four scans and the way macroporosity variation changes with height are shown in Fig. 11. The macroporosity is calculated by the average of the region with a height of 10 voxels. The macroporosity of the specimen in Scan 1 shows irregular fluctuation as the height changes, which is the result of the heterogeneity of the soil in the specimen. Drastic fluctuations in macroporosity are observed at the interface of the moist compacted soil layer (i.e., 50 mm and 100 mm). This indicates that the moist tamping method cannot produce completely uniform specimens and that the interface of the soil

layer suffers overcompaction or undercompaction (David Suits et al. 2003). The top and bottom of the specimen have higher macroporosity than its middle part, probably because some of the fine particles at the bottom are lost and the fine particles at the top settle downward under the effect of gravity in the saturation phase. According to a comparison regarding macroporosity between Scan 1 and Scan 2, there is no significant variation in overall macroporosity between the two, and no clear erosion occurs (Fig. 7), but a slight change in macroporosity is still observed in the vertical direction. The macroporosity of the upper and lower parts of the specimen slightly increases because a small amount of particles migrate downward under the seepage force. With the continuous development of seepage erosion, the macroporosity of both Scans 3 and 4 increases markedly over the entire height of the specimen. The macroporosity of the lower and middle parts of the specimen is far greater than that of the upper part, particularly in Scan 4. The macroporosity changes relatively uniformly between Scan 3 and Scan 2, while the macroporosity variation between Scan 4 and Scan 3 is mostly seen in the middle part of the specimen, and the lower part changes less (Fig. 11b). The main reason is that many of the fine particles in the lower part of the specimen are lost in the early stage of the test, and the content of fine particles susceptible to erosion decreases, while the middle part still has a high content of fine particles susceptible to erosion.

3.2.2 Macropore characteristics

Fig. 12 shows the measured characteristic parameters of macropores of the upper, middle and lower parts of the specimen and the average of the entire specimen in four scans. The parameters of different parts change differently because of the differences in soil structure and spatial position. The macroporosity and connected macroporosity of the specimen are the smallest in its middle part and the largest in its lower part. This is attributed to some of

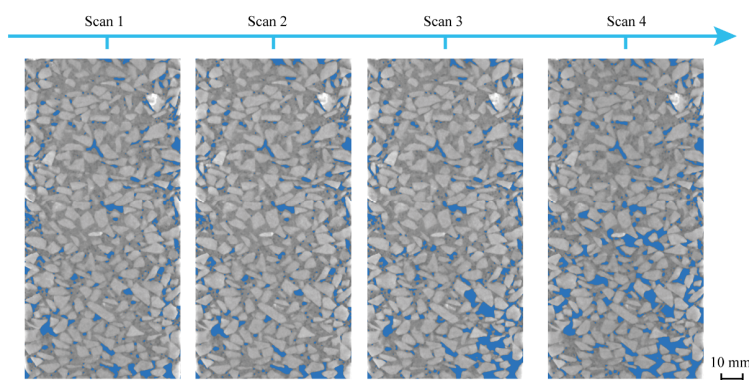


Fig. 8 Vertical sections in the median plane of the four scans.

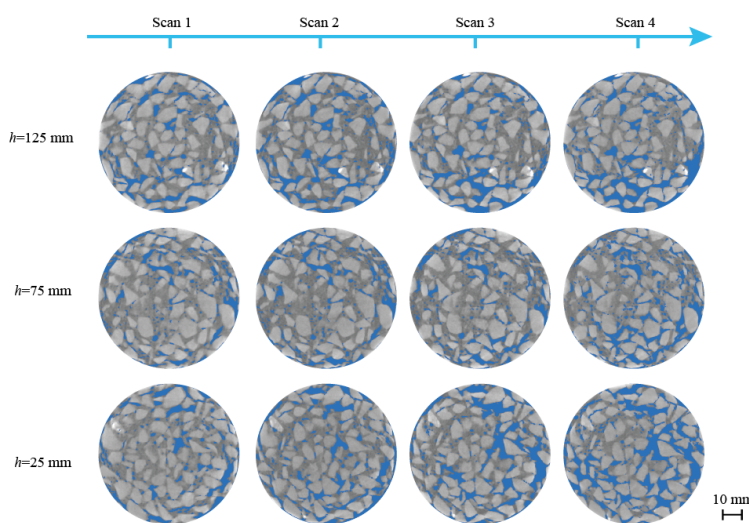


Fig. 9 Horizontal sections of the different height position of specimen with four scans. h is the height above base.

the fine particles in the upper part of the specimen moving downward to the middle part, and the loose soil particles in the lower part are lost during saturation. The macroporosity of each part of the specimen increases overall as a result of the continuous development of seepage erosion during the test. The macroporosity variation of each part is less between Scan 1 and Scan 2 and then increases significantly in subsequent scans (Scans 3 and 4). The upper part of the specimen has less variation in macroporosity. The connected macroporosity develops in a similar trend, except that the connected macroporosity increases relatively evidently in Scan 1 and Scan 2 in the middle part of the specimen.

The connected ratio of the lower part is significantly higher than that of the upper and middle parts. In Scan 1 and Scan 2, the connected ratio increases in the middle part of the specimen but

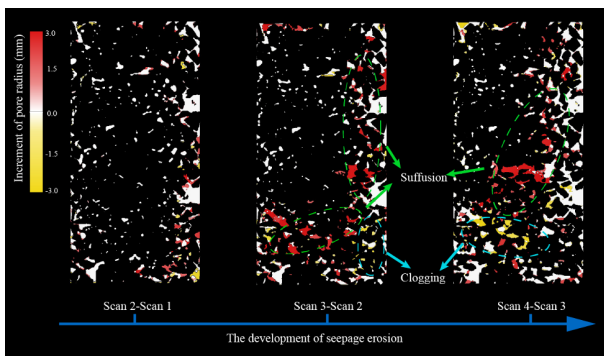


Fig. 10 Vertical cross-section of change of pore structure. Red macropores represent newly generated pores, and yellow macropores represent disappeared pores. White macropores represent unchanged pores between two scans.

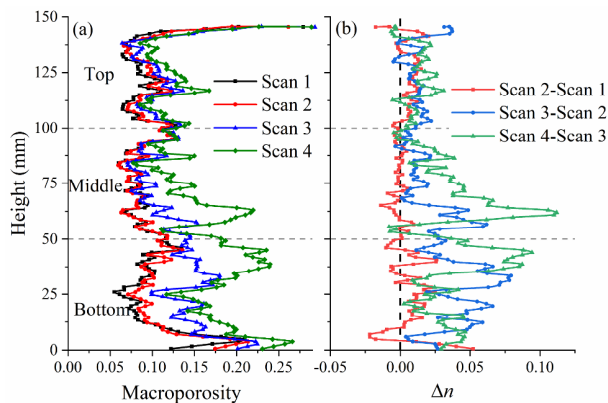


Fig. 11 Vertical profiles of (a) macroporosity and (b) increment of macroporosity of the four scans.

remains largely the same in the other parts. This is the reason that the hydraulic conductivity increases with the same macroporosity between Scans 1 and 2. The permeability of soil mainly depends on its connected pores (Wang et al. 2021a; Zhou and Li 2021). The middle part of the specimen has the least-connected macroporosity and plays a decisive role in water movement inside the soil. Therefore, as the connected ratio of the middle part of the specimen increases, the seepage channels increase, and thus, the permeability increases. In Scans 3 and 4, the connected ratio of the upper part of the specimen changes less, while the connected ratio of the middle and lower parts increases gradually. This is consistent with the change in the macroporosity of the specimen. This indicates that seepage erosion significantly affects the internal connectivity of soil. With the continuous migration and loss of fine particles resulting from the seepage force, the macropore structure of the soil subsequently changes. The pore size increases, the

pores become interconnected to provide preferential seepage channels, and the connectivity of the specimen increases accordingly.

The fractal dimension of each part of the specimen and the average fractal dimension of the entire specimen increase during the test. This is consistent with the conclusions of Peyton et al. (1994) and Shi et al. (2018), which indicated that there is a strong positive correlation between the fractal dimension of macropores and the macroporosity. Moreover, D_a can characterize the complexity and heterogeneity of the macropore structure. With the development of seepage erosion, there are clearly more macropores near the sidewall of the specimen than inside the specimen, and the macropores of the specimen are significantly nonuniformly distributed spatially (Figs. 8 and 9).

Compared with the upper and middle parts, the lower part of the specimen has a smaller specific surface area and higher average macropore diameter. The specific surface area of the specimen in Scan 2 changes slightly to that in Scan 1 and then decreases rapidly in Scan 3 and Scan 4, and the average macropore diameter of the specimen increases sharply after slight fluctuations. This is attributed to the pore diameter and specific surface area of porous media being generally negatively correlated. In addition, no clear development trend of the tortuosity of any part of the specimen is observed (Fig. 12). As seepage erosion develops, the pore shape factor of the upper and middle parts of the specimen gradually decreases, while that of the lower part slightly decreases in Scan 2 and then quickly increases (Scans 3 and 4). A possible explanation is that the lower part of the specimen has a higher degree of erosion, and the pores are interconnected to become columnar or bifurcated seepage channels that significantly change the shape of the macropores.

Fig. 13 shows the pore dip angle distribution during the seepage test. The dip angle is defined as the orientation of the pore long axis with respect to the horizontal plane, and it is the most direct parameter that reflects the pore orientation. In Scan 1, the macropores with dip angles of $5^\circ\sim 10^\circ$ account for the highest percentage of the total number of macropores, which is approximately 20.3%. The macropores with dip angles of $0^\circ\sim 45^\circ$ account for 92.5% of the total number of macropores, while the macropores with dip angles of $45^\circ\sim 90^\circ$ account for only 7.5%. This result indicates that the pore

orientation in the specimen is clearly anisotropic and that horizontal pores are dominant in the specimen. A possible reason for this distribution is the directional alignment of coarse particles during specimen preparation. The long axis of a coarse grain is mostly nearly horizontal under the effect of compaction, resulting in the small dip angle of the macropores

between grains ($< 45^\circ$). With the process of seepage erosion (Scans 1-4), the percentage of macropores with a $< 45^\circ$ dip angle gradually decreases, while that of macropores with a $> 45^\circ$ dip angle gradually increases from 7.5% to 10.9%. This is attributed to the migration of fine particles mostly occurring along the seepage direction (i.e., vertical direction in this study)

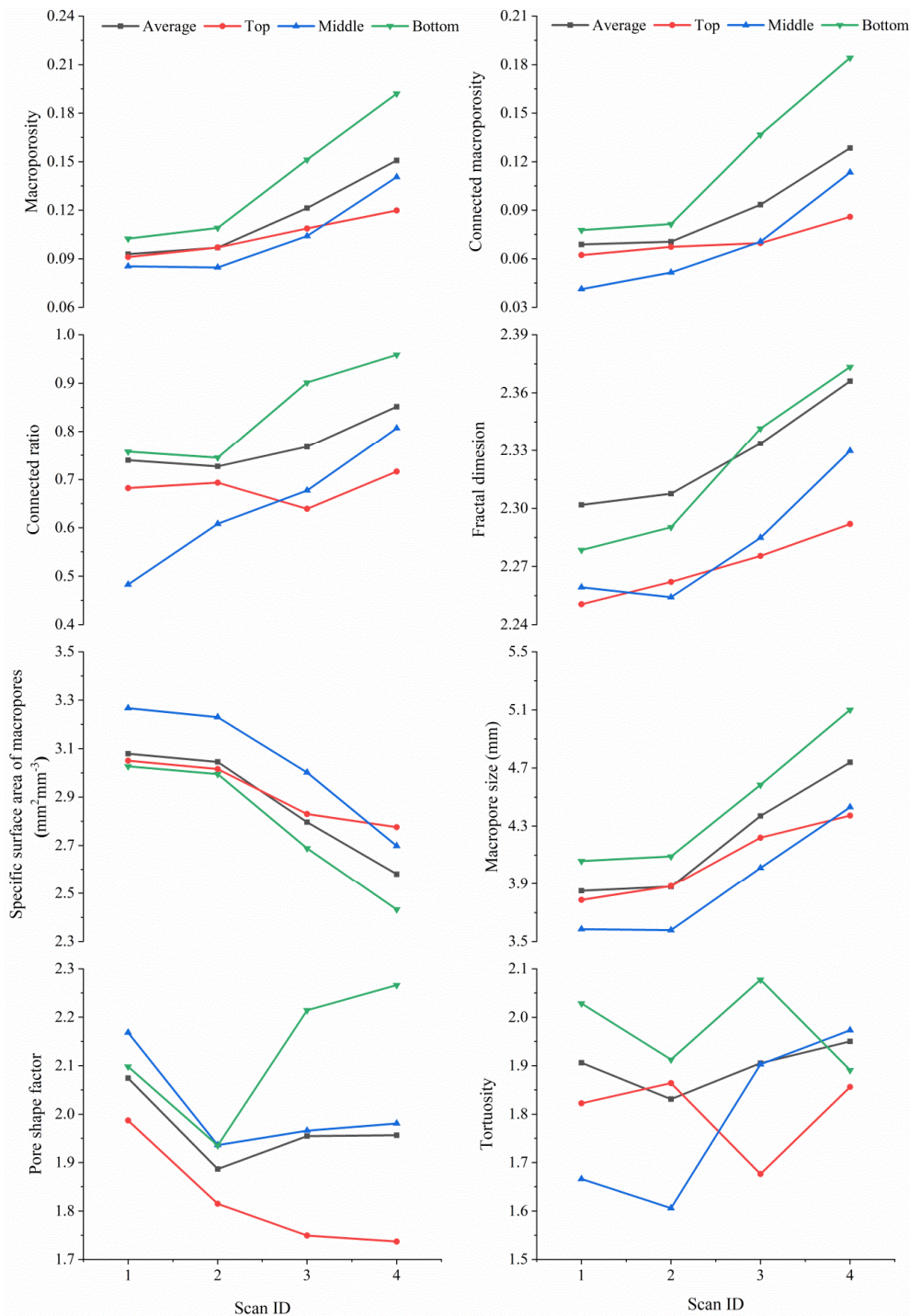


Fig. 12 Measured macropore characteristics of the different part of specimen in the four scans.

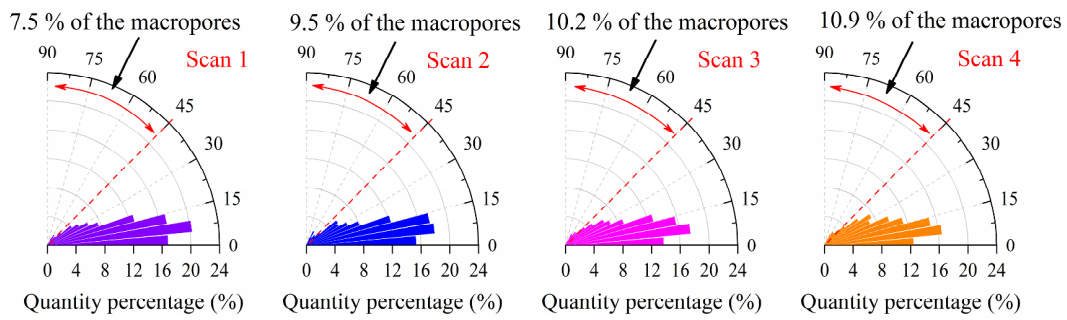


Fig. 13 Dig angle distribution in four scans.

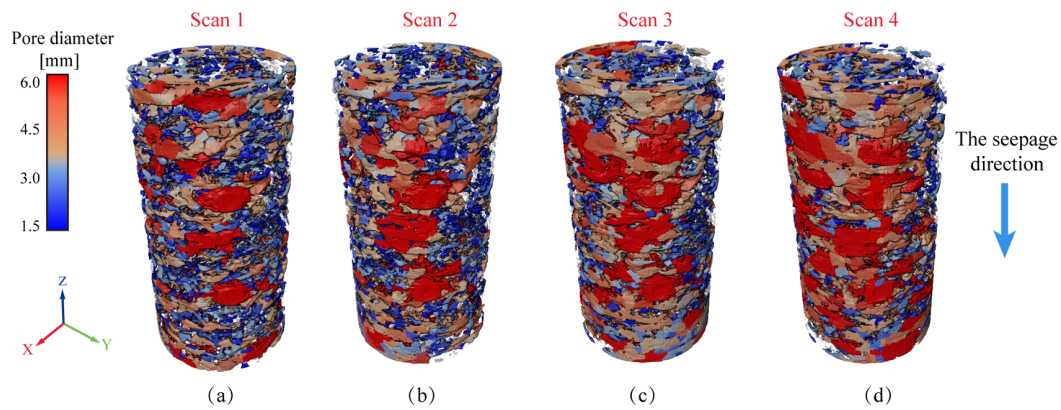


Fig. 14 Visualization of pore size distribution (PSD) in four scans.

and the macropores developing and merging along the vertical direction, resulting in a gradual increase in the pore dip angle. This also indicates that seepage erosion has a directional impact on pore development. The connectivity along the seepage direction in the soil will increase significantly, i.e., the formation of preferential seepage channels.

3.2.3 Pore size distribution (PSD)

Fig. 14 shows a visualization of the PSD of all the macropores in four scans, which indicates that the macropore size is significantly heterogeneous. There are fewer large macropores before the beginning of seepage erosion (Fig. 14a). With the progression of seepage erosion, the macropore distribution gradually changes. The pore size gradually increases, and the number of large macropores increases. The quantitative distribution and volume distribution of the equivalent pore size of each part of the specimen are shown in Figs. 15 and 16, which indicate the change in the macropores of the specimen during the seepage erosion test. The equivalent pore size quantitative distribution is unimodal. The macropores with 0.5–1 mm equivalent pore diameters account for the highest percentage of the total number of pores,

which is 30.5%~34%. The macropores with < 2 mm pore diameters account for 80.1%~85.9% of the total number of pores, which proves that most macropores of the specimen are within this range of equivalent pore diameters. As seepage erosion develops (Scans 1~4), the average pore quantitative distribution of the entire specimen shows no clear variation trend (Fig. 15a). This is possibly attributed to different parts of the specimen having different distributions of initial pore size, and seepage erosion developing nonuniformly between different parts of the specimen. In the early stage of the seepage test (Scans 1 and 2), the number of small macropores (diameter < 1 mm) in each part of the specimen increases, while the number and percentage of macropores with > 1 mm diameter both decrease to a certain extent. The macropores with diameters of 1~2 mm change the most obviously and are reduced by 2%. The reason is that the initial pore structure of the specimen has a high level of randomness during the saturation stage. Under the effect of seepage force, migration and clogging of some fine particles in the specimen are triggered, and some large pores are gradually filled or divided into small pores. With the process of seepage erosion (Scans 2~4), the number of small macropores

(diameter < 1 mm) decreases while the number of large macropores gradually increases. The quantity percentage of macropores with diameters > 2 mm increases the most significantly because the seepage erosion of the lower part of the specimen is most

severe.

The average pore volume distribution of the entire specimen is similar to a normal distribution (Fig. 16). The macropores with < 1 mm diameter account for the majority of all macropores, but their

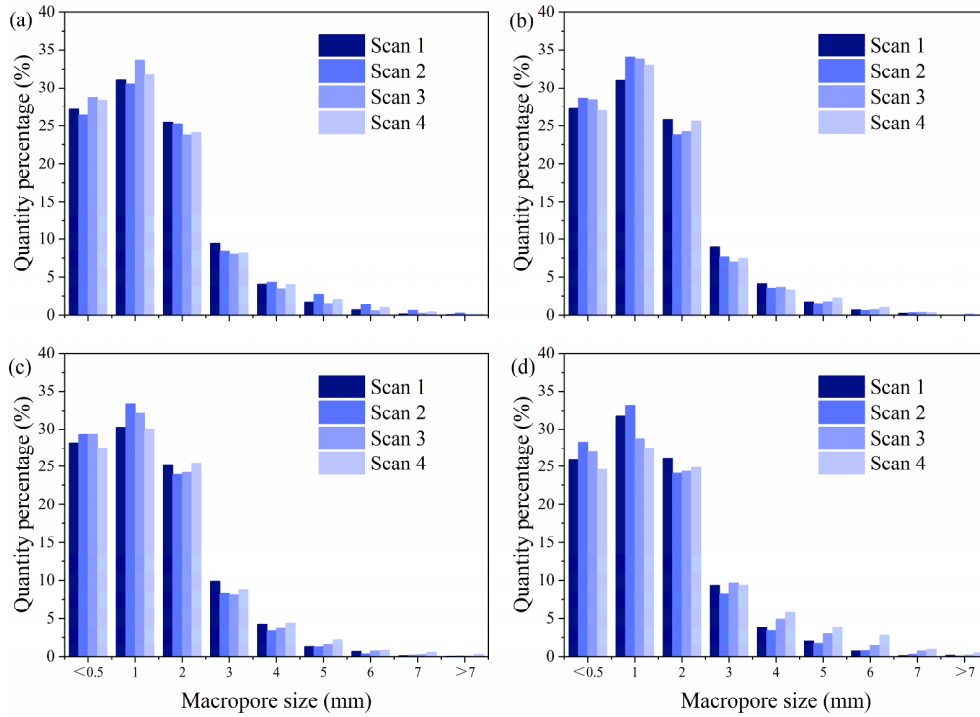


Fig. 15 Pore size distribution (by quantity) in the four scans. (a) Average; (b) Top; (c) Middle; (d) Bottom.

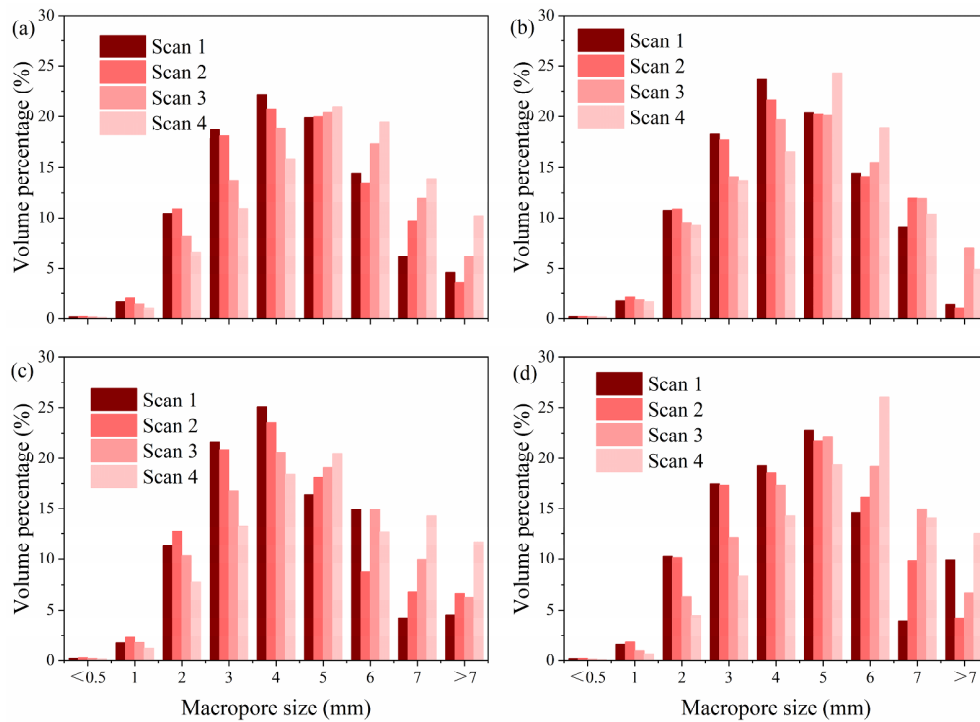


Fig. 16 Pore size distribution (by volume) in the four scans. (a) Average; (b) Top; (c) Middle; (d) Bottom.

volume percentage is very low. In comparison, the large macropores develop an opposite trend. In the initial macropore structure (Scan 1), macropores with diameters of 3–4 mm account for the highest volume percentage, which is approximately 22%. With the evolution of seepage erosion, the volume percentage of macropores with diameters of 0–4 mm gradually decreases, while that of pores with diameters > 4 mm gradually increases. At the end of the test, the volume percentage of the > 4 mm macropores is 64.5%, which is 1.5 times the value at the beginning of the test. The pore volume distribution of the upper and middle parts of the specimen shows a similar evolution trend to the average of that of the entire specimen, while the change in the pore volume distribution of the lower part of the specimen is slightly different. The loss of fine particles in the lower part of the specimen is serious, and thus, the pores merge into larger pores easily. The volume percentage of macropores with a diameter of 4–5 mm decreases with the seepage erosion process, and that of macropores > 5 mm in diameter increases significantly. The percentage of macropores of the upper part of the specimen with a diameter greater than 6 mm is approximately 10.7% at the end of the test, which is significantly lower than that of the middle and lower parts of the specimen. This might be due to the heterogeneity of the soil structure of the specimen and the relatively lower extent of erosion in the upper part of the specimen.

To conduct a more in-depth and detailed investigation and understanding of the pore distribution conditions during seepage erosion, several parameters were extracted and employed to characterize the change in the pore distribution according to the PSD curve (Fig. 17). The coefficient of nonuniformity (C_{pu}) and coefficient of curvature (C_{pc}) of PSD are defined similar to C_u and C_c of GSD, which can describe properties of pore distribution. A larger value of C_{pu} indicates a more nonuniform distribution of pore size in the soil and a wider range of PSD. C_{pc} reflects the continuity of PSD, which increases with the increase in large pores.

$$\begin{cases} C_{pu} = \frac{d_{p60}}{d_{p10}} \\ C_{pc} = \frac{(d_{p30})^2}{d_{p60} \times d_{p10}} \end{cases} \quad (1)$$

where d_{p10} , d_{p30} and d_{p60} are the pore sizes corresponding to 10%, 30%, and 60% of the pores by volume, respectively.

Soils composed of grains and pores with different sizes exhibit fractal characteristics, and numerous

fractal dimensions have been proposed to describe the distribution characteristics of grain and pore sizes. The pore fractal dimension (D_p) is a statistical fractal dimension that is suitable and convenient for characterizing the entire pore distribution properties (Zhou et al. 2016; Feng et al. 2020). D_p can reflect the relationship between the microstructure characteristics of soil and macroparameters such as the GSD, permeability, and density. The fractal relationship of the PSD can be expressed by

$$\frac{V(<r)}{V_T} = \left(\frac{r}{r_{max}}\right)^{3-D_p} \quad (2)$$

where $V(<r)$ is the cumulative volume of pores with sizes smaller than a certain size r , V_T is the total volume of the specimen, r is the given comparative pore size, and r_{max} is the maximum pore size of the sample.

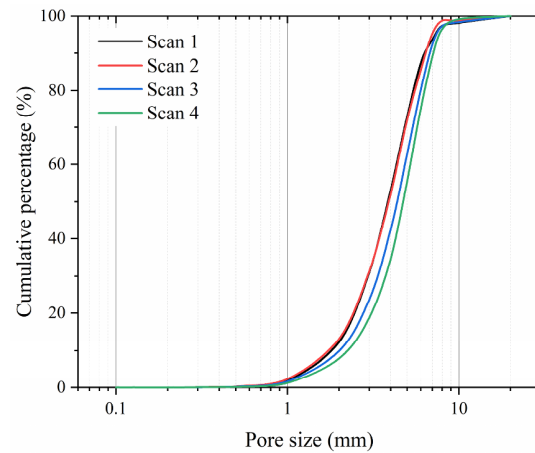


Fig. 17 Curves of pore size distribution in four scans

Hence, the value of the pore fractal dimension can be calculated as follows:

$$D_p = 3 - \frac{\ln(V(<r)/V_T)}{\ln(r/r_{max})} \quad (3)$$

The pore fractal dimensions and characteristic pore sizes of different scans are shown in Table 3. The pore fractal dimension has an obvious negative correlation with the coefficient of nonuniformity, suggesting that D_p can be used to characterize the PSD in this study. When the hydraulic gradient is low (Scan 1 to Scan 2), the characteristic pore sizes show slight variations, and d_{p10} and d_{p30} slightly decrease while d_{p60} increases. Moreover, C_{pu} increases from 2.40 to 2.53, and D_p decreases from 2.624 to 2.612, indicating an increase in both small sized and large sized pores in the soil and a more uneven distribution of pores. With increasing hydraulic gradient (Scan 2 to Scan 4), the fine particles are gradually lost, and

Table 3 Properties of macropore distribution in the four scans

	Hydraulic gradient	d_{p10} (mm)	d_{p30} (mm)	d_{p50} (mm)	d_{p60} (mm)	C_{pu}	C_{pc}	D_p
Scan 1	0.0	1.80	2.95	3.85	4.32	2.40	1.12	2.624
Scan 2	0.82	1.73	2.93	3.88	4.38	2.53	1.13	2.612
Scan 3	1.41	2.01	3.36	4.37	4.84	2.41	1.16	2.621
Scan 4	1.80	2.24	3.74	4.74	5.21	2.32	1.20	2.632

the overall pore size increases. C_{pu} decreases from 2.53 to 2.32, and C_{pc} and D_p gradually increases from 1.13 and 2.612 to 1.20 and 2.632, respectively. This indicates that the range of pore sizes narrows and that the PSD becomes more uniform and continuous with the development of seepage erosion.

Based on Fig. 18, D_p has a significant quadratic relationship with the hydraulic gradient. This is because the seepage erosion process is a dynamic process in which fine particle migration and clogging continuously alter the soil. According to the change in PSD distribution and macroscopic phenomenon during the seepage erosion test (Fig. 7 and Fig. 18), the evolution of macropore structure can be divided into two stages:

Initiation phase (corresponding to Scan 1 to Scan 2, $i = 0 \sim 0.8$): when the hydraulic gradient is lower than the critical hydraulic gradient, a small amount of loose soil particles around the macropores are more vulnerable to migration, resulting in an increase in the volume of the large pores; meanwhile, these migrating particles are prone to deposition and clogging in the seepage channel due to the lower seepage force, which causes some pores to split into smaller pores, and the pore distribution tends to be more nonuniform. In this phase, the rearrangement of soil particles mainly occurs inside the soil without significant erosion loss, and the soil microstructure is

not damaged substantially. The values of the characteristic pore sizes show slight fluctuations. C_{pu} increases and D_p decreases with increasing hydraulic gradient.

Erosion phase (corresponding to Scan 2 to Scan 4, $i = 0.8 \sim 1.8$): all characteristic pore sizes as well as D_p increases significantly, but C_{pu} decreases. This is because fine particle migration is dominant in this phase, and the loss of fine particles increases gradually with increasing hydraulic gradient. Small pores rapidly expand or merge into large pores, leading to a decrease in the unevenness of the PSD.

3.2.4 Characterization of connected macropores

The pores in the soil consist of independent pores and connected pores. Connected pores are the actual transmission channels of water in soil, which control the permeability of the soil. Therefore, it is essential to investigate the properties of connected pores. The PNM can accurately determine the size and spatial distribution of connected pores and can better extract the characteristics of connected pore structures (Gharedaghloo et al. 2018; He et al. 2020). The pore size characteristics of connected pores comprise the connected pore radius, throat length, throat radius and coordination number, which is intuitive and convenient for obtaining the connectivity and connected pore space structure of the specimen. Fig. 19 shows the PNM of the specimen in four scans. The pores and throats are characterized by a ball-and-stick model, in which the spheres represent the pores and the cylinder represents the throats. The size and position of a sphere and cylinder reflect the size and position of an actual pore and throat, respectively. Fig. 19 indicates that the PNM is inhomogeneous even before the seepage erosion test (Fig. 19a). Some large pores are distributed in the periphery of the specimen, suggesting the presence of a potentially preferential seepage channel. During the seepage test, the PNM structure shows a gradual local change. The sizes of the pores and throats increase slowly, resulting in the development of preferential seepage channels (Fig. 19c). With the development of

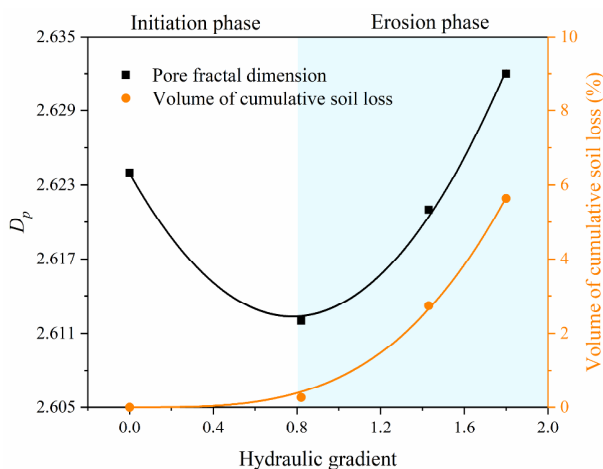


Fig. 18 Variations in D_p and cumulative soil loss with hydraulic gradient.

seepage erosion, the preferential seepage channel gradually extends and forms the concentrated erosion zone (Fig. 19d).

Fig. 20 shows the quantitative statistics of the PNM, including the connected pore radius, throat radius and throat length. The pore radius distribution is unimodal with a peak value of 1 mm. With the process of seepage erosion, the variation trend of the connected pore radius distribution is similar to that of the total PSD. The peak value of the distribution of the throat radius and length appeared at 0.5 mm for throat radius and 5 mm for throat length. The quantity percentage of throats with throat radii ≥ 1.5 mm to all total throats increases, and the percentage of throats with throat radii ≤ 0.5 mm decreases during the seepage erosion process, resulting in a decrease in flow resistance and an increase in soil permeability (Fig. 7). The throat length is mainly distributed in the range of 2.5~10 mm, and the number of throats included in this range accounts for 88.5~91.2% of all throats (Fig. 20c). When the throat length ranges from 5~10 mm, the proportion of throats gradually increases with the development of seepage erosion.

The coordination number is one of the essential parameters that represent the connectivity of the soil pore structure. Usually, a greater coordination number entails better connectivity. Fig. 21 shows the coordination number of each part of the specimen and the average coordination number of the entire specimen. The pores with a coordination number of < 5 account for 85.1% of the total number of macropores of the entire specimen (Fig. 21a). As seepage erosion develops, the percentage of macropores with a coordination number of < 5 gradually decreases, while that of macropores with a coordination number of > 5 gradually increases. At the end of the test, the percentage of macropores with a coordination number of > 5 is 25%, which increases by approximately 1.7 times. This proves that the macropore structure of the specimen becomes more complex as a result of seepage erosion. The seepage channels increase during the test, the movement of water is made easier, and the permeability subsequently increases. The coordination number of the middle and lower parts of the specimen and that of the entire specimen change in essentially the same

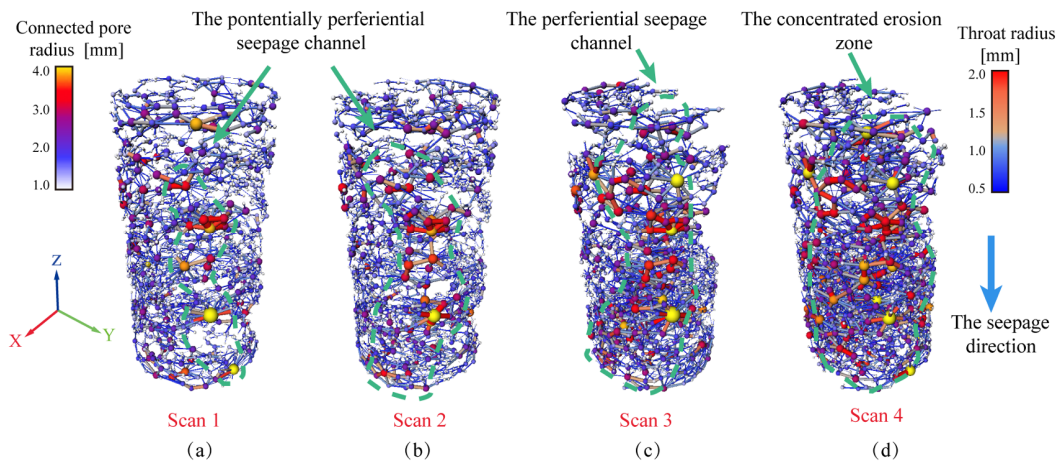


Fig. 19 Visualization of the pore network model (PNM) in four scans.

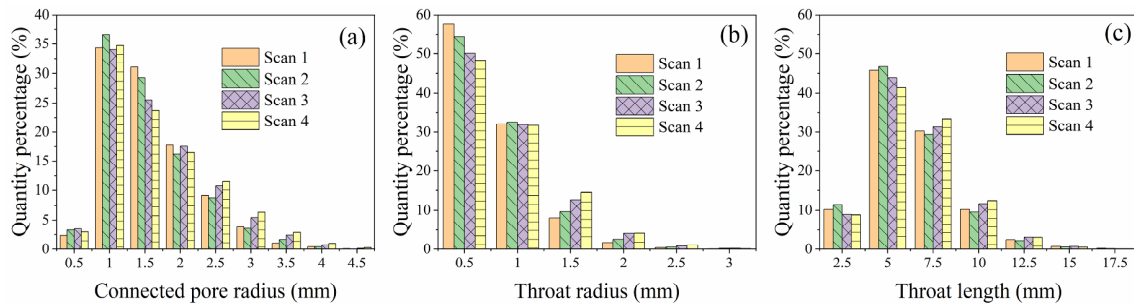


Fig. 20 Quantitative statistics of pore and throat characteristics of the PNM. (a) Connected pore radius; (b) Throat radius; (c) Throat length.

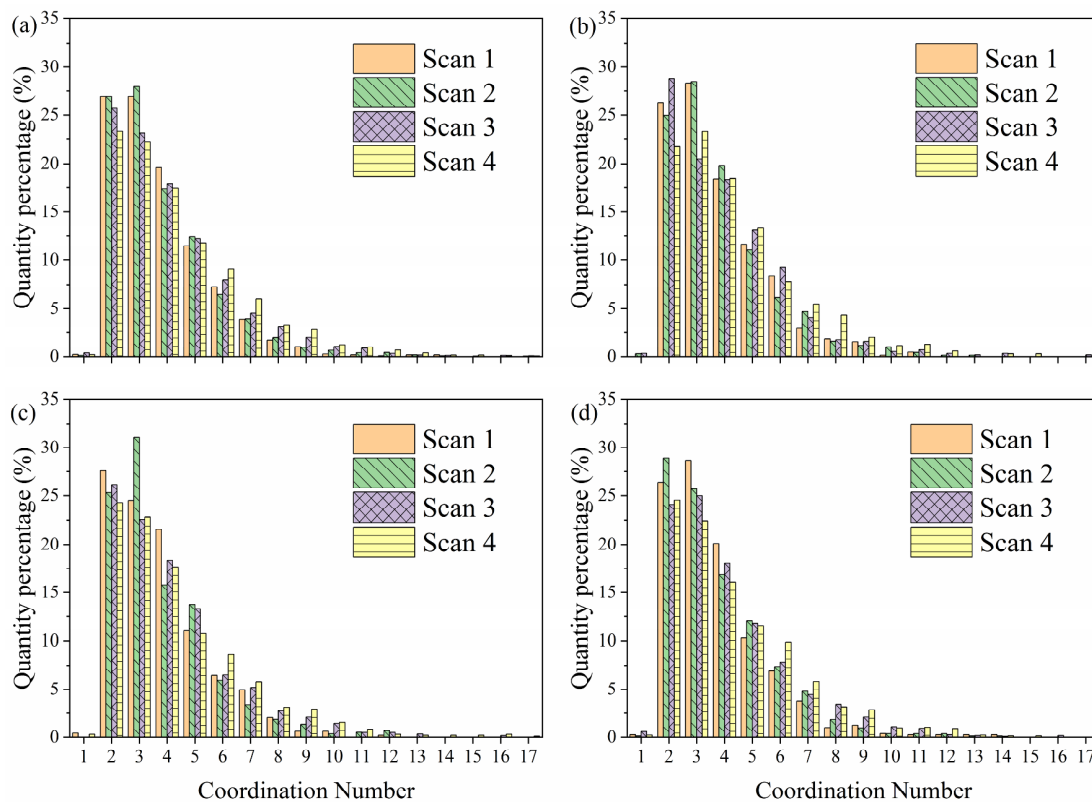


Fig. 21 Coordination number distribution in the four scans. (a) Average; (b) Top; (c) Middle; (d) Bottom.

trend. For the upper part of the specimen, the coordination number distribution shows no noticeable variation trend during the test except that the macropores with a coordination number > 7 increase at the end of the test (Scan 4). This proves that the macropore structure of the upper part of the specimen changes less and is less affected by seepage erosion.

Notably, the macropores quantitatively analyzed in this study are only a part of the overall pore of the soil. To quantitatively analyze smaller pores in soil, smaller samples or higher-resolution CT equipment is necessary to obtain higher-resolution images. However, a more representative sample size was employed in this study considering the soil structure and seepage conditions, and the decrease in the sample size may have an impact on the soil structure. In addition, high-resolution CT scanning equipment is still rare, and scanning and image processing require considerable time and high costs (Schlüter et al. 2014; Zhao et al. 2020). Therefore, further studies on the combination of CT scanning with other test methods (such as nuclear magnetic resonance) and improvement of image processing methods are needed to achieve quantitative analyses of pores with

different pore sizes and enhance the accuracy of the test results.

3.3 Relationship between permeability and macropore structure characteristics

Macropores are the main flow channels of water in soil, and their structure is the most critical factor affecting the permeability of soil. Hence, it is essential to investigate the relationship between macropore structure characteristics and soil permeability. Fig. 22 shows the correlation analysis between the macropore structure characteristics and soil permeability in this study. The soil permeability is positively correlated with macropores, connected macropores, fractal dimension, coordination number and macropore size, and the fitted correlation coefficients are all above 0.85. There is the highest positive correlation between permeability and coordination number, indicating that changes in connectivity have a significant effect on soil permeability during the seepage erosion process. Moreover, the correlations of soil permeability with the specific surface area of macropores and macropore size are also significantly strong during the seepage erosion process. The soil

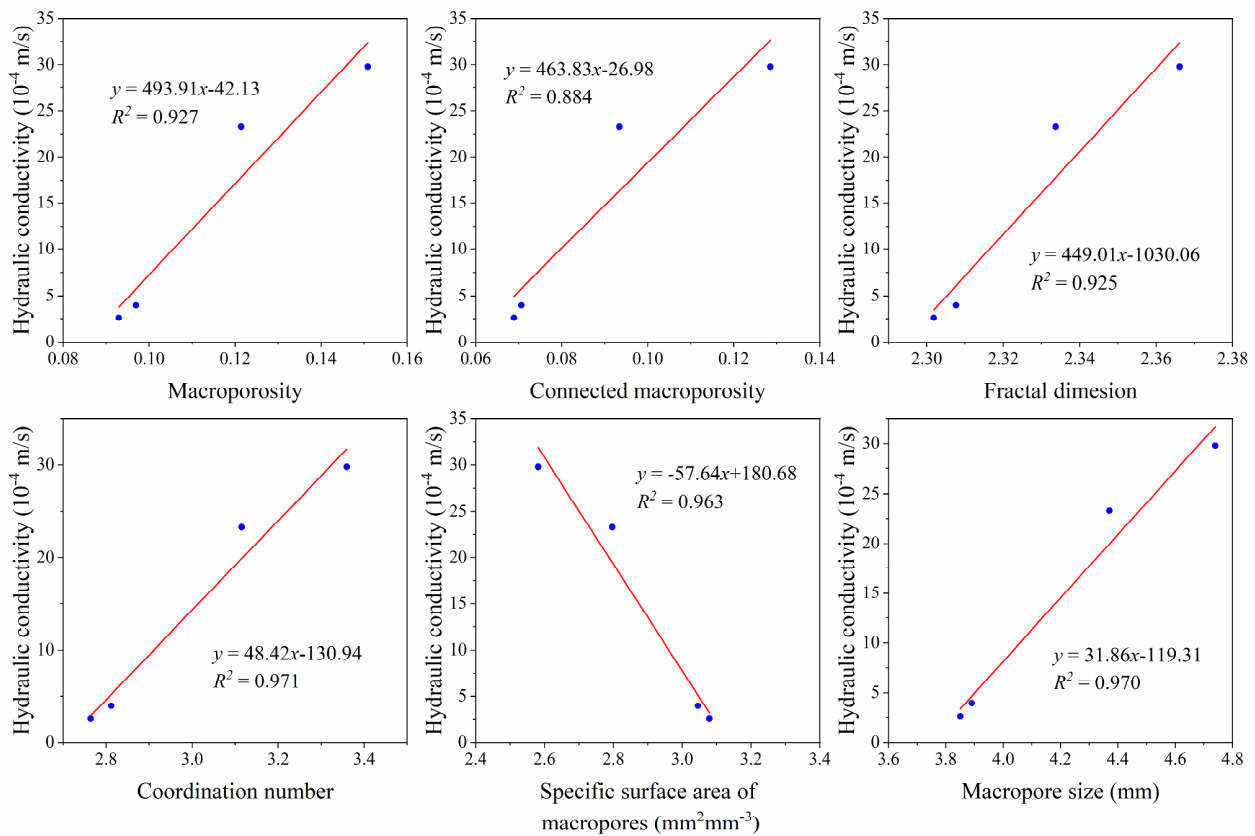


Fig. 22 Correlation between soil permeability and macropore structure characteristics.

permeability is negatively correlated with the specific surface area of macropores and positively correlated with the macropore size. This is because the specific surface area of macropores and macropore size determine the resistance of water flow in the soil. The decrease in the specific surface area of macropores and the increase in macropore size lead to easier transportation of water, suggesting an increase in permeability.

3.4 Seepage erosion effects on soil deformation

The results of CT scanning indicate that the development of seepage erosion and its influence on the changes in soil structure and pore distribution show obvious heterogeneity, which is closely related to spatial location. The extent of erosion is most severe downstream of the seepage direction (i.e., the lower part of the specimen), especially near the seepage outlet. During the evolution of seepage erosion, the macroporosity and connectivity of the soil at the downstream part are higher, implying a lower soil strength. The downstream part is more prone to

deformation and settlement due to seepage. Local mechanical tests cannot be conducted on such tests, but the results can be verified by an analysis of grayscale images using digital volume correlation (DVC). The DVC method can obtain the strain field and displacement field before and after deformation with CT images and is widely applied in material mechanics, biomechanics, and geotechnical fields (Shi et al. 2021). A detailed description of the DVC method can be found in Kak et al. (2002) and Li et al. (2020). Based on Fig. 23, the deformation of the

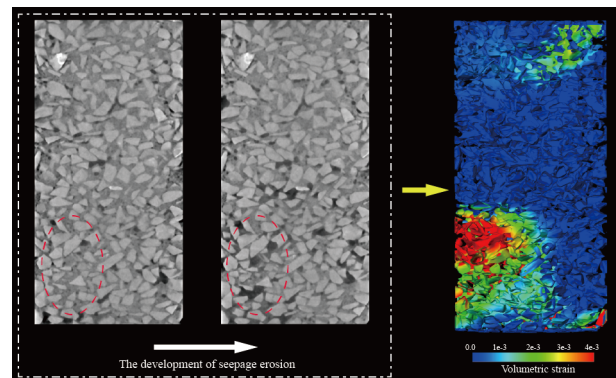


Fig. 23 Vertical cross-section of grayscale images and strain field.

specimen is severely inhomogeneous and inconsecutive. Obvious settlement and deformation of the overall specimen are not observed. However, the soil at the lower part of the specimen, especially near the sidewall of the specimen, shows prominent settlement. The maximum local strain can reach 0.38%. Hence, seepage-induced disasters, such as dam cracking, bank slump and hydrodynamic pressure landslides, are often triggered preferentially at the downstream zone of seepage in engineering practice.

4 Conclusions

In this study, the changes in macropore structure and soil deformation during the seepage erosion test are investigated with CT scanning. The influences of seepage erosion on macropore characteristics are quantitatively studied. The PNM of the specimen is extracted, and the evolution of the connected pore size characteristics is discussed. The following conclusions are drawn based on the results:

1) The initial pore distribution inside the specimen is heterogeneous due to microstructural stratification induced by the moist tamping method and the presence of the edge effect. The macropores are more concentrated on the periphery than in the center of the specimen.

2) The changes in macropore characteristics are significantly influenced by seepage erosion. The macroporosity, average macropore size, connectivity and fractal dimension of the soil rapidly increase with the development of seepage erosion. Moreover, the macropore orientation gradually deviates toward the seepage direction, and the connectivity of macropores increases with seepage erosion, resulting in an increase in permeability.

3) The PSD of the soil is unimodal. The evolution of the PSD can be divided into an initiation phase and an erosion phase. In the initiation phase, the characteristic pore sizes fluctuate slightly, and the pore distribution becomes more nonuniform with increasing hydraulic gradient; in the erosion phase, the small pores become larger and fuse into larger pores due to the loss of fine particles, resulting in an overall increase in pore size and a gradual uniformity in PSD. The pore fractal dimension D_p shows a significant quadratic relationship with the hydraulic gradient, indicating that it can better reflect the

changes in soil microstructural characteristics. It is helpful to accurately assess the erosion degree and the evolution of the macropore structure of the localized soil during the seepage erosion process.

4) The influence of seepage erosion on macropore characteristics and soil deformation is heterogeneous and closely dependent on the spatial location of the soil. More precisely, the loss of fine particles and change in macropore characteristics are most significant downstream of seepage. The pronounced heterogeneities of seepage erosion should be considered in engineering practice, which significantly changes the hydraulic and mechanical properties of local soil and might affect the stability of geotechnical engineering.

Acknowledgments

The work is supported by the National Natural Science Foundation of China (No. 41972297) and the Natural Science Foundation of Hebei Province (No. D2021202002).

Author Contribution

All authors contributed to the study conception and design. Material preparation, data collection and analysis were performed by Huang Da, Huang Wen-bo and Gao Yi-kang. The first draft of the manuscript was written by Huang Wen-bo. The previous versions were reviewed and edited by Huang Da. All authors commented on previous versions of the manuscript and all authors read and approved the final manuscript.

Ethics Declaration

Availability of Data/Materials: Some or all data, models, or code that support the findings of this study are available from the corresponding author upon reasonable request.

Conflict of Interest: The authors declare that they have no known competing financial interests or personal relationships that could have appeared to influence the work reported in this paper.

References

- Bendahmane F, Marot D, Alexis A (2008) Experimental parametric study of suffusion and backward erosion. *J Geotech Geoenviron Eng* 134: 57-67.
[https://doi.org/10.1061/\(ASCE\)1090-0241\(2008\)134:1\(57\)](https://doi.org/10.1061/(ASCE)1090-0241(2008)134:1(57))
- Bianchi F, Wittel FK, Thielmann M, et al. (2018) Tomographic study of internal erosion of particle flows in porous media. *Transp Porous Media* 122: 169-184.
<https://doi.org/10.1007/s11242-017-0996-8>
- Buczko U, Bens O, Huttel RE (2006) Tillage effects on hydraulic properties and macroporosity in silty and sandy soils. *Soil Sci Soc Am J* 70: 1998-2007.
<https://doi.org/10.2136/sssaj2006.0046>
- Budhathoki S, Lamba J, Srivastava P, et al. (2022) Using X-ray computed tomography to quantify variability in soil macropore characteristics in pastures. *Soil Tillage Res* 215: 105194. <https://doi.org/10.1016/j.still.2021.105194>
- Chang DS, Zhang LM (2013) Critical hydraulic gradients of internal erosion under complex stress states. *J Geotech Geoenviron Eng* 139: 1454-1467.
[https://doi.org/10.1061/\(ASCE\)GT.1943-5606.0000871](https://doi.org/10.1061/(ASCE)GT.1943-5606.0000871)
- Cheik S, Bottinelli N, Minh TT, et al. (2019) Quantification of three dimensional characteristics of macrofauna macropores and their effects on soil hydraulic conductivity in northern Vietnam. *Front Environ Sci* 7
<https://doi.org/10.3389/fenvs.2019.00031>
- Chen L, Wan Y, He JJ, et al. (2021) Experimental study on the suffusion mechanism of gap-graded soils under an exceedance hydraulic gradient. *Nat Hazards* 109: 405-439.
<https://doi.org/10.1007/s11069-021-04842-2>
- Chu-Agor ML, Fox GA, Cancienne RM, et al. (2008) Seepage caused tension failures and erosion undercutting of hillslopes. *J Hydrol* 359: 247-259.
<https://doi.org/10.1016/j.jhydrol.2008.07.005>
- Crosta G, Prisco CD (1999) On slope instability induced by seepage erosion. *Can Geotech J* 36: 1056-1073.
- Daneshian B, Habibagahi G, Nikoee E (2021) Determination of unsaturated hydraulic conductivity of sandy soils: a new pore network approach. *Acta Geotech* 16: 449-466.
<https://doi.org/10.1007/s11440-020-01088-3>
- David Suits L, Sheahan TC, Frost JD, et al. (2003) A critical assessment of the moist tamping technique. *Geotech Test J* 26: 57-70. <https://doi.org/10.1520/gtj11108j>
- Dragila MI (2005) Principles of soil physics. *Vadose Zone J* 4: 448-448. <https://doi.org/10.2136/vzj2004.0012br>
- Fan N, Wang JR, Deng CB, et al. (2020) Quantitative characterization of coal microstructure and visualization seepage of macropores using CT-based 3D reconstruction. *J Nat Gas Sci Eng* 81.
<https://doi.org/10.1016/j.jngse.2020.103384>
- Fannin RJ, Moffat R (2006) Observations on internal stability of cohesionless soils. *Geotechnique* 56: 497-500.
<https://doi.org/10.1680/geot.56.7.497>
- Fell R, Fry JJ (2007) *Internal erosion of dams and their foundations*. Crc Press.
- Feng SX, Chai JR, Xu ZG, et al. (2020) Test study on the suffusion process of sand-rock mixtures by NMR systems. *Geotech Test J* 43: 1286-1299.
<https://doi.org/10.1520/Gtj20180208>
- Flores-Berrones R, Ramirez-Reynaga M, Macari J (2011) Internal erosion and rehabilitation of an earth-rock dam. *J Geotech Geoenviron Eng* 137: 150-160.
[https://doi.org/10.1061/\(ASCE\)GT.1943-5606.0000371](https://doi.org/10.1061/(ASCE)GT.1943-5606.0000371)
- Foster M, Fell R, Spannagle M (2000) The statistics of embankment dam failures and accidents. *Can Geotech J* 37: 1000-1024. <https://doi.org/10.1139/t00-030>
- Gharedaghloo B, Price JS, Rezanezhad F, et al. (2018) Evaluating the hydraulic and transport properties of peat soil using pore network modeling and X-ray micro computed tomography. *J Hydrol* 561: 494-508.
<https://doi.org/10.1016/j.jhydrol.2018.04.007>
- Guo CX, Cui YF (2020) Pore structure characteristics of debris flow source material in the Wenchuan earthquake area. *Eng Geol* 267. <https://doi.org/10.1016/j.enggeo.2020.105499>
- He K, Ye C, Deng Y, et al. (2020) Study on the microscale structure and anti-seepage properties of plastic concrete for cut-off walls modified with silica fume: experiment and modelling. *Constr Build Mater* 261
<https://doi.org/10.1016/j.conbuildmat.2020.120489>
- Hu C, Liu XL, Jia YG, et al. (2020) Permeability anisotropy of methane hydrate-bearing sands: insights from CT scanning and pore network modelling. *Comput Geotech* 123
<https://doi.org/10.1016/j.compgeo.2020.103568>
- Huang D, Gu DM (2017) Influence of filling-drawdown cycles of the Three Gorges reservoir on deformation and failure behaviors of anacinal rock slopes in the Wu Gorge. *Geomorphology* 295: 489-506.
<https://doi.org/10.1016/j.geomorph.2017.07.028>
- Huang D, Gu DM, Song YX, et al. (2018) Towards a complete understanding of the triggering mechanism of a large reactivated landslide in the Three Gorges reservoir. *Eng Geol* 238: 36-51. <https://doi.org/10.1016/j.enggeo.2018.03.008>
- Huang D, Huang W-B, Ke C-Y, et al. (2021) Experimental investigation on seepage erosion of the soil-rock interface. *Bull Eng Geol Environ* 80: 3115-3137.
<https://doi.org/10.1007/s10064-021-02104-w>
- Huang D, Luo SL, Zhong Z, et al. (2020) Analysis and modeling of the combined effects of hydrological factors on a reservoir bank slope in the Three Gorges reservoir area, China. *Eng Geol* 279: 105858.
<https://doi.org/10.1016/j.enggeo.2020.105858>
- Huang RQ (2009) Some catastrophic landslides since the twentieth century in the southwest of China. *Landslides* 6: 69-81. <https://doi.org/10.1007/s10346-009-0142-y>
- Jarvis NJ (2020) A review of non-equilibrium water flow and solute transport in soil macropores: principles, controlling factors and consequences for water quality. *Eur J Soil Sci* 71: 279-302. <https://doi.org/10.1111/ejss.12973>
- Kak AC, Slaney M, Wang G (2002) Principles of computerized tomographic imaging. *Medical Physics* 29: 107-107.
<https://doi.org/10.1118/1.1455742>
- Ke L, Takahashi A (2014) Experimental investigations on suffusion characteristics and its mechanical consequences on saturated cohesionless soil. *Soils Found* 54: 713-730.
<https://doi.org/10.1016/j.sandf.2014.06.024>
- Kenney TC, Lau D (1985) Internal stability of granular filters. *Canadian Geotechnical Journal* 22:420-423.
- Kezdi A (1979) *Soil Physics: Developments in Geotechnical Engineering*. Elsevier Science Ltd., Amsterdam, Netherlands
- Kido R, Higo Y, Takamura F, et al. (2020) Morphological transitions for pore water and pore air during drying and wetting processes in partially saturated sand. *Acta Geotech* 15: 1745-1761.
<https://doi.org/10.1007/s11440-020-00939-3>
- Kim HJ, Park JM, Shin JH (2019) Flow behaviour and piping potential at the soil-structure interface. *Geotechnique* 69: 79-84. <https://doi.org/10.1680/jgeot.17.T.020>
- Korup O (2004) Geomorphometric characteristics of New Zealand landslide dams. *Eng Geol* 73: 13-35.
<https://doi.org/10.1016/j.enggeo.2003.11.003>
- Lei X-q (2021) Two-dimensional finite element modeling of seepage-erosion coupled process within unsaturated soil slopes. *J Mt Sci* 19: 446-460.
<https://doi.org/10.1007/s11629-021-6776-5>
- Li CS, Kong LW, Shu RJ, et al. (2020) Dynamic three-dimensional imaging and digital volume correlation analysis to quantify shear bands in grus. *Mech Mater* 151: 14.
<https://doi.org/10.1016/j.mechmat.2020.103646>
- Li X, Lu YD, Zhang XZ, et al. (2019) Quantification of

- macropores of Malan loess and the hydraulic significance on slope stability by X-ray computed tomography. *Environ Earth Sci* 78: 522-521-522-519.
<https://doi.org/10.1007/s12665-019-8527-2>
- Lin HS, McInnes KJ, Wilding LP, et al. (1995) Effective porosity and flow rate with infiltration at low tensions into a well-structured subsoil. *International Symposium on Water Quality Modeling*. pp 435-448.
- Liu M, Zhang Y, Tian SF, et al. (2020) Effects of loose deposits on debris flow processes in the Aizi Valley, southwest China. *J Mt Sci* 17: 156-172.
<https://doi.org/10.1007/s11629-019-5388-9>
- Liu WP, Wan SF, Huang FM, et al. (2019) Experimental study of subsurface erosion in granitic under the conditions of different soil column angles and flow discharges. *Bull Eng Geol Environ* 78: 5877-5888.
<https://doi.org/10.1007/s10064-019-01519-w>
- Luo LF, Lin H, Li SC (2010) Quantification of 3-D soil macropore networks in different soil types and land uses using computed tomography. *J Hydrol* 393: 53-64.
<https://doi.org/10.1016/j.jhydrol.2010.03.031>
- Manahiloh KN, Meehan CL (2017) Determining the soil water characteristic curve and interfacial contact angle from microstructural analysis of X-ray CT images. *J Geotech Geoenviron Eng* 143.
[https://doi.org/10.1061/\(asce\)gt.1943-5606.0001677](https://doi.org/10.1061/(asce)gt.1943-5606.0001677)
- Meng C, Niu JZ, Yin ZC, et al. (2018) Characteristics of rock fragments in different forest stony soil and its relationship with macropore characteristics in mountain area, northern China. *J Mt Sci* 15: 519-531.
<https://doi.org/10.1007/s11629-017-4638-y>
- Moffat R, Fannin RJ, Garner SJ (2011) Spatial and temporal progression of internal erosion in cohesionless soil. *Can Geotech J* 48: 399-412. <https://doi.org/10.1139/T10-071>
- Nguyen CD, Benahmed N, Ando E, et al. (2019) Experimental investigation of microstructural changes in soils eroded by suffusion using X-ray tomography. *Acta Geotech* 14: 749-765.
<https://doi.org/10.1007/s11440-019-00787-w>
- Nowamooz H, Jahangir E, Masroufi F, et al. (2016) Effective stress in swelling soils during wetting drying cycles. *Eng Geol* 210: 33-44. <https://doi.org/10.1016/j.enggeo.2016.05.021>
- Pan P, Shang Y-q, Lü Q, et al. (2017) Periodic recurrence and scale-expansion mechanism of loess landslides caused by groundwater seepage and erosion. *Bull Eng Geol Environ* 78: 1143-1155. <https://doi.org/10.1007/s10064-017-1090-8>
- Peyton RL, Gantzer CJ, Anderson SH, et al. (1994) Fractal dimension to describe soil macropore structure using X ray computed tomography. *Water Resour Res* 30: 691-700.
<https://doi.org/10.1029/93wr02343>
- Qin ZP, Lai YM, Tian Y, et al. (2021) Effect of freeze-thaw cycles on soil engineering properties of reservoir bank slopes at the northern foot of Tianshan Mountain. *J Mt Sci* 18: 541-557.
<https://doi.org/10.1007/s11629-020-6215-z>
- Richards KS, Reddy KR (2007) Critical appraisal of piping phenomena in earth dams. *Bull Eng Geol Environ* 66: 381-402. <https://doi.org/10.1007/s10064-007-0095-0>
- Richards KS, Reddy KR (2012) Experimental investigation of initiation of backward erosion piping in soils. *Geotechnique* 62: 933-942. <https://doi.org/10.1680/geot.11.P.058>
- Sail Y, Marot D, Sibille L, et al. (2011) Suffusion tests on cohesionless granular matter experimental study. *Eur J Environ Civ Eng* 15: 799-817.
<https://doi.org/10.3166/Ejece.15.799-817>
- Schlüter S, Sheppard A, Brown K, et al. (2014) Image processing of multiphase images obtained via X-ray microtomography: a review. *Water Resour Res* 50: 3615-3639.
<https://doi.org/10.1002/2014wr015256>
- Shi HL, Hosdez J, Rougelot T, et al. (2021) Analysis of local creep strain field and cracking process in claystone by X-ray micro-tomography and digital volume correlation. *Rock Mech Rock Eng* 54: 1937-1952.
<https://doi.org/10.1007/s00603-021-02375-5>
- Shi X, Pan J, Hou Q, et al. (2018) Micrometer-scale fractures in coal related to coal rank based on micro-CT scanning and fractal theory. *Fuel* 212: 162-172.
<https://doi.org/10.1016/j.fuel.2017.09.115>
- Simms P, Yanful E (2005) A pore-network model for hydromechanical coupling in unsaturated compacted clayey soils. *Can Geotech J* 42: 499-514.
<https://doi.org/10.1139/t05-002>
- Starkloff T, Larsbo M, Stolte J, et al. (2017) Quantifying the impact of a succession of freezing-thawing cycles on the pore network of a silty clay loam and a loamy sand topsoil using X-ray tomography. *Catena* 156: 365-374.
<https://doi.org/10.1016/j.catena.2017.04.026>
- Suits LD, Sheahan TC, Chang DS, et al. (2011) A stress-controlled erosion apparatus for studying internal erosion in soils. *Geotech Test J* 34.
<https://doi.org/10.1520/gtj103889>
- Videla A, Lin C-L, Miller JD (2006) Watershed functions applied to a 3D image segmentation problem for the analysis of packed particle beds. *Part Part Syst Charact* 23: 237-245.
<https://doi.org/10.1002/ppsc.200601055>
- Wan CF, Fell R (2008) Assessing the potential of internal instability and suffusion in embankment dams and their foundations. *J Geotech Geoenviron Eng* 134: 401-407.
[https://doi.org/10.1061/\(Asce\)1090-0241\(2008\)134:3\(401\)](https://doi.org/10.1061/(Asce)1090-0241(2008)134:3(401))
- Wang G, Qin XJ, Han DY, et al. (2021a) Study on seepage and deformation characteristics of coal microstructure by 3D reconstruction of CT images at high temperatures. *Int J Min Sci Technol* 31: 175-185.
<https://doi.org/10.1016/j.ijmst.2020.11.003>
- Wang G, Qin XJ, Shen JN, et al. (2019) Quantitative analysis of microscopic structure and gas seepage characteristics of low-rank coal based on CT three-dimensional reconstruction of CT images and fractal theory. *Fuel* 256
<https://doi.org/10.1016/j.fuel.2019.115900>
- Wang HM, Ni WK, Yuan KZ, et al. (2021b) Microstructure evolution of loess under multiple collapsibility based on nuclear magnetic resonance and scanning electron microscopy. *J Mt Sci* 18: 2612-2625.
<https://doi.org/10.1007/s11629-021-6838-8>
- Zhao D, Xu MX, Liu GB, et al. (2017) Quantification of soil aggregate microstructure on abandoned cropland during vegetative succession using synchrotron radiation-based micro-computed tomography. *Soil Tillage Res* 165: 239-246.
<https://doi.org/10.1016/j.still.2016.08.007>
- Zhao Y, Hu X, Li X (2020) Analysis of the intra-aggregate pore structures in three soil types using X-ray computed tomography. *Catena* 193.
<https://doi.org/10.1016/j.catena.2020.104622>
- Zhou HW, Zhong JC, Ren WG, et al. (2018) Characterization of pore-fracture networks and their evolution at various measurement scales in coal samples using X-ray μ CT and a fractal method. *International Journal of Coal Geology* 189: 35-49. <https://doi.org/10.1016/j.coal.2018.02.007>
- Zhou S, Liu D, Cai Y, et al. (2016) Fractal characterization of pore-fracture in low-rank coals using a low-field NMR relaxation method. *Fuel* 181: 218-226.
<https://doi.org/10.1016/j.fuel.2016.04.119>
- Zhou XP, Li CQ (2021) Permeability prediction of porous geomaterials subjected to freeze-thaw cycles based on 3D reconstruction technology. *Cold Reg Sci Tech* 181.
<https://doi.org/10.1016/j.coldregions.2020.103180>
- Zhu Q, Su LJ, Liu ZY, et al. (2022) An evaluation method for internal erosion potential of gravelly soil based on particle size distribution. *J Mt Sci* 19: 1203-1214.
<https://doi.org/10.1007/s11629-021-7115-6>
- Zuo L, Xu L, Baudet BA, et al. (2020) The structure degradation of a silty loess induced by long-term water seepage. *Eng Geol* 272. <https://doi.org/10.1016/j.enggeo.2020.105634>